

Probing the pseudocapacitance and energy-storage performance of RuO₂ facets from first principles

Nathan Keilbart,^{1,*} Yasuaki Okada,² and Ismaila Dabo¹

¹*Department of Materials Science and Engineering, Materials Research Institute, and Penn State Institutes of Energy and the Environment, The Pennsylvania State University, University Park, Pennsylvania 16802, USA*

²*Murata Manufacturing Co., Ltd., 1-10-1, Higashikotari, Nagaokakyo-shi, Kyoto 617-8555, Japan*



(Received 3 June 2019; published 23 August 2019)

The energy density of ruthenia (RuO₂) pseudocapacitor electrodes is critically dependent on their surface structure. To understand this dependence, we simulate the electrochemical response of RuO₂(110), RuO₂(100), and RuO₂(101) in aqueous environments using a self-consistent continuum solvation (SCCS) model of the solid-liquid interface. The insertion of protons into the RuO₂(110) sublayer is found to profoundly affect the voltage-dependent characteristics of the system, leading to a sharp transition from a battery-type to capacitor-type response. The calculated charge-voltage properties for RuO₂(101) are in qualitative agreement with experiment, albeit with a pseudocapacitance that is significantly underestimated. In contrast, the RuO₂(100) facet is correctly predicted to be pseudocapacitive over a wide voltage window, with a calculated pseudocapacitance in close agreement with experimental voltammetry. These results establish the SCCS model as a reliable approach to predict and optimize the facet-dependent pseudocapacitance of polycrystalline systems.

DOI: [10.1103/PhysRevMaterials.3.085405](https://doi.org/10.1103/PhysRevMaterials.3.085405)

I. INTRODUCTION

Pseudocapacitive materials operate through fast and reversible reactions that occur near the electrode-electrolyte interface. These mechanisms allow for high charging rates which are desirable in high-power applications, such as kinetic energy harvesting and pulse power in electronic devices [1–3]. To model pseudocapacitive charge storage from first principles, it is important to consider the environmental factors that control the response of the interface. Such considerations include the voltage-dependent polarization of the solvent and the multiple adsorption structures that contribute to the temperature-dependent configurational entropy of the system. Simulations have shown promise in predicting the energy capacity of pseudocapacitive interfaces from first principles [4–10], but further systematic comparative assessments are required to ensure the transferability of these models. Ruthenia (RuO₂), a prototypical pseudocapacitor material, is chosen here to critically examine the predictive accuracy of our recently proposed model [6].

The cyclic voltammogram (CV) of polycrystalline RuO₂ electrodes exhibits a nearly rectangular profile with various facets contributing distinct features to the overall voltammetric response [11–14]. By integrating the area under the voltammogram, a pseudocapacitance of 700–1500 F/g is typically measured [15,16]. In this work, we apply a voltage-dependent computational approach to probe the pseudocapacitive response of the individual RuO₂ facets. Due to the electrochemical nature of pseudocapacitive energy storage, embedded electronic-structure calculations based on density-functional theory (DFT) and the self-consistent continuum

solvation (SCCS) model of Andreussi *et al.* [17] are used to simulate the redox reactions that enable pseudocapacitive charge storage. Temperature-dependent sampling techniques are also applied to capture the critical influence of entropic contributions [6,8–10,18–22] with a focus on the (110), (100), and (101) crystallographic planes.

This work is organized as follows. We first present the quantum-continuum method to predict the electronic-structure properties of the electrochemical interface. We then present a grand canonical Monte Carlo sampling technique and explain the large-scale calculation of the surface energies. We conclude by comparing the predicted trends to experimental data for each surface facet to assess the predict performance and transferability of the model.

II. COMPUTATIONAL METHODS

A. Quantum-continuum modeling

Electronic-structure calculations are carried out using the PW code of the QUANTUM-ESPRESSO computational suite [23]. The generalized gradient approximation under the Perdew-Burke-Ernzerhof (PBE) parametrization [24] is applied to describe electron-electron interactions. Ultrasoft pseudopotentials are employed to describe the ionic cores. Kinetic energy and charge density cutoffs for the plane-wave expansion are set to 50 and 500 Ry, respectively. The Marzari-Vanderbilt cold smearing method [25] with a broadening energy of 0.03 Ry is employed to smoothen the occupations of the electronic states. The lattice constants of the bulk crystal are calculated to be $a = 4.5 \text{ \AA}$ and $c = 3.1 \text{ \AA}$ [6].

The solvent environment is modeled using the SCCS model [17,26]. In this approach, the transition of the dielectric permittivity of the solvent is expressed in terms of the charge

*nathan.keilbart@psu.edu

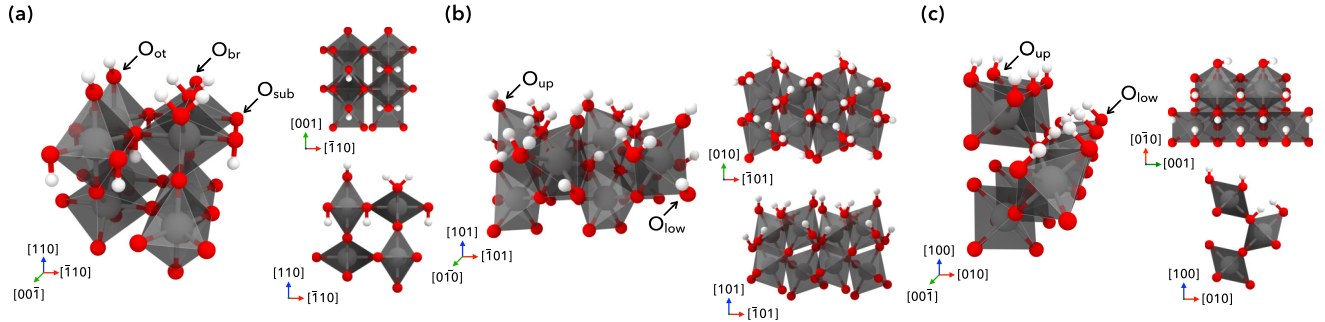


FIG. 1. Different views of the RuO_2 surface facets with the fully relaxed geometry of the adsorbed protons. (a) For the (110) facet, protons sit on the on-top O_{ot} and bridging O_{br} sites of the exposed layer with additional adsorption sites within the first sublayer O_{sub} . (b) For the (101) facet, surface oxygen sites are occupied by protons until reaching an occupancy of two protons per surface oxygen. As seen in the top and side view, the two oxygens facing down also show the possibility of proton adsorption. (c) (100) facet has eight sites split between an upper O_{up} and lower O_{low} adsorption site. Upper sites are located at the protruding polyhedra while the lower adsorption sites sit within a channel created by these upper polyhedra.

density as $\epsilon = \exp\{[\zeta - \sin(2\pi\zeta)/2\pi] \ln \epsilon_0\}$, where ϵ_0 is the dielectric constant of the bulk solvent and ζ is defined as $\zeta = (\ln \rho_{\text{max}} - \ln \rho) / (\ln \rho_{\text{max}} - \ln \rho_{\text{min}})$ with $\rho_{\text{max}} = 5 \times 10^{-3}$ a.u. and $\rho_{\text{min}} = 10^{-4}$ a.u. representing the charge density cutoffs that define the internal and external isocontours of the smooth dielectric cavity. Additionally, nonelectrostatic contributions such as the external pressure and surface tension, as well as dispersion and repulsion effects, are included. These contributions are modeled as $G_{\text{cav}} = \gamma S$ and $G_{\text{dis+rep}} = \alpha S + \beta V$, where $\gamma = 72$ dyn/cm is the experimental solvent surface tension, and $\alpha = -22$ dyn/cm and $\beta = -0.35$ GPa are fitted parameters. Here S and V are the quantum surface and volume of the solute that are defined as $S = -\int d\mathbf{r} \theta[\rho(\mathbf{r})] |\nabla \rho(\mathbf{r})|$ and $V = \int d\mathbf{r} \theta[\rho(\mathbf{r})]$, which involve the smooth switching function $\theta(\rho) = [\epsilon_0 - \epsilon(\rho)] / (\epsilon_0 - 1)$. Finally, we align the potential of the system to the reference electrostatic energy deep within the bulk dielectric region, allowing us to calculate an potential of zero charge (PZC) and determine the voltage of the charged surface.

B. Surface structures

A slab model of the RuO_2 (100) and (101) facets is created with a 2×1 and 1×1 unit cell comprising eight and six oxygen adsorption sites, respectively. The adsorption energies are found to be converged with an accuracy of 50 meV for the four-layer slab structure. To eliminate spurious electrostatic interactions between the periodic surface dipoles, the supercells are constructed to be symmetric with respect to the center of the slab. The hydrogens are placed on both sides of the slab with a minimum vacuum height of 10 Å between the periodic images. The Brillouin zone is sampled using a Monkhorst-Pack $2 \times 2 \times 1$ grid.

There are several possible surface terminations available for the two orientations, but as suggested by several studies [5,13,27–29], the surface is terminated by oxygen in contact with an aqueous environment. Thus an oxygenated surface is used for both the (100) and (101) facets. It is important to note that the possibility of oxygen vacancies do exist but to keep the amount of configurations within a computationally tractable number, pristine surfaces are used through the course

of this study. The previously calculated surface termination for the (110) facet [6], shown in Fig. 1(a), is adopted to construct additional configurations, investigating the possibility of subsurface adsorption sites in the first sublayer of the material. Increasing amounts of subsurface protons are placed below oxygens until a maximum of four protons are inserted within the sublayer. Several configurations of the sublayer are used to comprehensively capture the configurational possibilities. A total of 66 symmetrically unique structures are considered in the dataset which is expanded to 494 configurations by applying symmetry operations.

The (101) surface has most of the adsorption sites located at the surface. By examining the ruthenium-centered octahedra shown in Fig. 1(b), it is seen that the protons preferentially orient towards the surface facing oxygens. When the upper sites are populated, lower oxygen sites on the same octahedra become more favorable energetically.

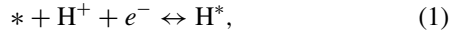
The (100) surface consists of two upper and two lower oxygens that serve as sites for a total of eight adsorption possibilities on the 2×1 surface where the lower sites sit within a tunnel that is located at the surface, as shown in Fig. 1(c). Hydrogens are positioned near each of these sites and allowed to relax in contact with the continuum solvent. As the hydrogen adsorbs onto the higher of the two upper sites, they orient towards the next oxygen. When the surface is fully protonated, the hydrogen on the other upper site prefers to sit directly above the oxygen. For the lower sites the hydrogens point toward the oxygen atoms located above the adsorption site and face away from the ruthenium atom located nearby as can be seen in Fig. 1(c). Using these placements, 256 configurations are enumerated and the total number of calculations is reduced to 125 with the use of symmetry operations.

C. Finite-temperature electrochemistry

Current electronic-structure methods based on DFT are applicable for systems of relatively small size (typically, a few hundreds of electrons) due to the cubic scaling of the computational complexity as a function of the number of electrons. Hence, extrapolation methods are needed to explore

the configurational space of an extended surface. Our extrapolation method is explained below.

The chemical reaction to be modeled is



where $*$ represents a free site on the surface, H^+ is a proton in solution, e^- is an electron that reduces the proton at the surface, and H^* is the proton adsorbed at the specified site. This methodology is used to simulate a single adsorption event or several adsorption processes at once where the pristine surface serves as the reference.

The energy of the system is expanded into a charge-dependent second-order Taylor series:

$$\mathcal{E}(Q, N_{\text{H}}) = \mathcal{E}(0, N_{\text{H}}) + \Phi_0 Q + \frac{Q^2}{2C_0}, \quad (2)$$

where the first term $\mathcal{E}(0, N_{\text{H}})$ is the adsorption energy of the species on the surface that is computed as $\mathcal{E}(0, N_{\text{H}}) = \mathcal{E}_0(N_{\text{H}}) - \mathcal{E}_0(0) - N_{\text{H}} \mu_{\text{H}^+ + e^-}$ with $\mathcal{E}_0(N_{\text{H}})$ being the total energy of the adsorption system, $\mathcal{E}_0(0)$ denoting the reference energy with no adsorbate, and $\mu_{\text{H}^+ + e^-}$ being the joint chemical potential of the proton and electron. In Eq. (2), Φ_0 denotes the PZC of the system that is evaluated by immersing the electrode in the continuum electrolyte and aligning the electrostatic potential to a common reference, which enables us to write

$$\Phi_0 = -\frac{(\varepsilon_{\text{F}})_0}{e_0}, \quad (3)$$

where $(\varepsilon_{\text{F}})_0$ is the Fermi energy of the neutral system and e_0 is the elementary charge. The final term in Eq. (2) is the double-layer response of the system, computed by applying a varying charge to the system and taking the derivative of the resulting Fermi energies as a function of the surface charge. As the system acquires a positive or negative charge, a compensating charge is introduced at 3 Å from the surface to represent the response of Helmholtz countercharges. This procedure allows us to calculate the differential capacitance of the system:

$$C = \frac{\partial Q}{\partial \Phi}, \quad (4)$$

where $\Phi = -\varepsilon_{\text{F}}/e_0$ is the applied voltage of the charged electrode. This representation of the energy is adequate for systems exhibiting a linear response for Eq. (4) but would require additional terms for a nonlinear response. Additional contributions to the energy include the chemical potential dependence of the adsorbing protons that is a function of the pH, chemical potential of the electron, and potential of the electrode as established in the computational hydrogen electrode approach [30–33]. The expression for the additional environmental terms can be written as

$$\mu_{\text{H}^+ + e^-} = \frac{1}{2} \mu_{\text{H}_2}^\circ - k_{\text{B}} T \ln(10) \text{pH} + e_0 (\Phi - \Phi_{\text{SHE}}^\circ), \quad (5)$$

where $\mu_{\text{H}_2}^\circ$ is the chemical potential of a hydrogen molecule under standard state conditions, the second term is the concentration dependence of the proton in solution, and Φ_{SHE}° is the standard redox potential of the proton in solution.

As mentioned in Sec. II B, there are many configurational states for the adsorbates. To sample all the possibilities of the

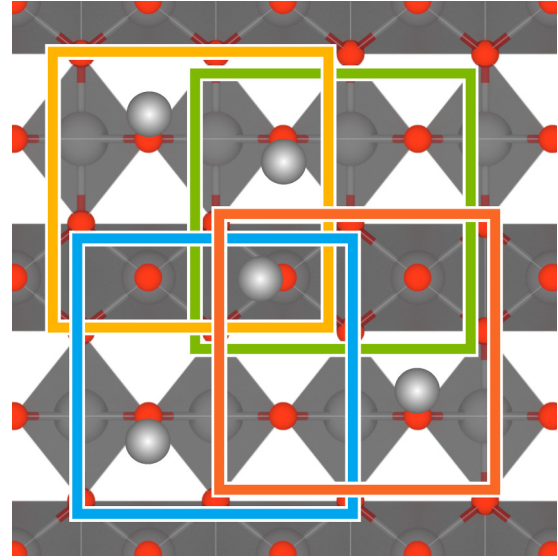


FIG. 2. The energy extrapolation is performed by summing the contributions from each of the 2×2 unit cells that overlap on a given adsorption site. The calculation is then repeated for each of the adsorption sites to provide an averaged estimate of the total energy.

configurational space, grand canonical Markov chain Monte Carlo is used with the modified free energy described in Eqs. (2) and (5) that accounts for the applied potential and the activity of the protons in solution.

The computational method is developed in Ref. [6]; here we give a brief review of its key features. The framework consists of averaging the free energy of the different surface cells that overlap at a given adsorption site. The dependence of the free energy as a function of the charge reads

$$\mathcal{E} = \frac{1}{16} \sum_j \sum'_\alpha \mathcal{E}^\alpha, \quad (6)$$

where the energy is summed over all sites j in the first summation and then summed over the different surface configurations α that overlap at site j , as illustrated in Fig. 2. The method of Eq. (6) is then applied to randomly sample the configurations under varying environmental conditions, following the Metropolis-Hastings acceptance probability

$$\mathcal{P} = \begin{cases} 1, & \text{if } \Delta \mathcal{E} < 0, \\ e^{-\frac{\Delta \mathcal{E}}{k_{\text{B}} T}}, & \text{if } \Delta \mathcal{E} > 0. \end{cases} \quad (7)$$

The results of the sampling are reported in the following section.

III. RESULTS AND DISCUSSION

We first discuss the grand canonical Monte Carlo simulations of the (110), (101), and (100) surfaces as a function of the applied voltage. The dataset of computed electrochemical properties is reported in Tables A1–A4 of the Supplemental Material [34].

The simulations for the surface orientations are then parametrized from these results. The supercell consists of 20×20 adsorption sites or 10×10 unit cells. The voltage ranges from 0 to 1.6 V vs SHE with a step of 0.01 V at

a constant temperature of 300 K. The pH is set to be 0.3 to reproduce the electrolytic conditions at a concentration of 0.5 M H_2SO_4 [11,35,36]. Each site is given an average of 200 attempts during the sampling (corresponding to more than 80 000 total attempts) and each property is averaged over 100 full Monte Carlo runs. A detailed analysis of the resulting responses and adsorption isotherms is given below for each surface orientation.

A. $RuO_2(110)$

It has been suggested that there exist *outer* and *inner* adsorption regions for RuO_2 [2,5,37–40]. The outer region is defined as the collection of adsorption sites situated directly at the interface while the inner region comprises the adsorption sites that are located within the first sublayer where diffusion to the surface is still probable. By accessing the inner region, the effective area of the pseudocapacitor is increased leading to a higher energy capacity.

Previous calculations of the $RuO_2(110)$ surface examining the outer region demonstrated good agreement with experiment [6,11]. Further calculations were performed enumerating the possible configurations at the inner adsorption sites near the surface of the material. As mentioned in Sec. II, all surface configurations were recomputed with an increasing amount of subsurface protons. This yields 66 symmetrically unique configurations which are listed in Tables A1 and A2 [34].

The inclusion of subsurface adsorption in the grand canonical model translates into an even broader variety of capacitor-type charge-voltage responses. In fact, it is seen in Fig. 3(a) that all the sensitivity-analysis simulations with fixed double-layer capacitance C_0 yield a gradual depletion of the surface that is in contrast with the behavior observed in the absence of subsurface adsorption and suggests the onset of pseudocapacitive charge storage.

By allowing the subsurface protons to freely exchange during the simulation, different amounts of subsurface occupancies are observed at a varying double-layer capacitance as shown in Fig. 3(b). Similar trends are observed for double-layer capacitances from 0 to $10 \mu F/cm^2$ which show an initial subsurface population of 0.04 protons per site while a higher capacitance of $20 \mu F/cm^2$ leads to 0.11 protons per site. All double-layer capacitances show a linear response with respect to the voltage and appear to discharge all subsurface protons at ~ 0.9 V vs SHE. Our previous results with no sublayer adsorption indicate that the constant capacitance of $10 \mu F/cm^2$ is in good agreement with experimental results [6]. Upon comparing the subsurface adsorption results with the experimental trend, there is a deviation over lower voltage range of 0–1.0 V when the same capacitance of $10 \mu F/cm^2$ is used. Although there are less than 0.4 protons/site in the sublayer, they provide a stabilizing force to the other adsorbed protons causing a delay in their desorption. Additionally, the double-layer capacitance of $10 \mu F/cm^2$ recovers the experimental trend at ~ 1.0 V which is approximately where the subsurface layer completely deprotonates. The charged surface model of the outer adsorption region, shown in Fig. 5(a), exhibit nearly identical slopes as the experimental measurements yielding similar capacitances.

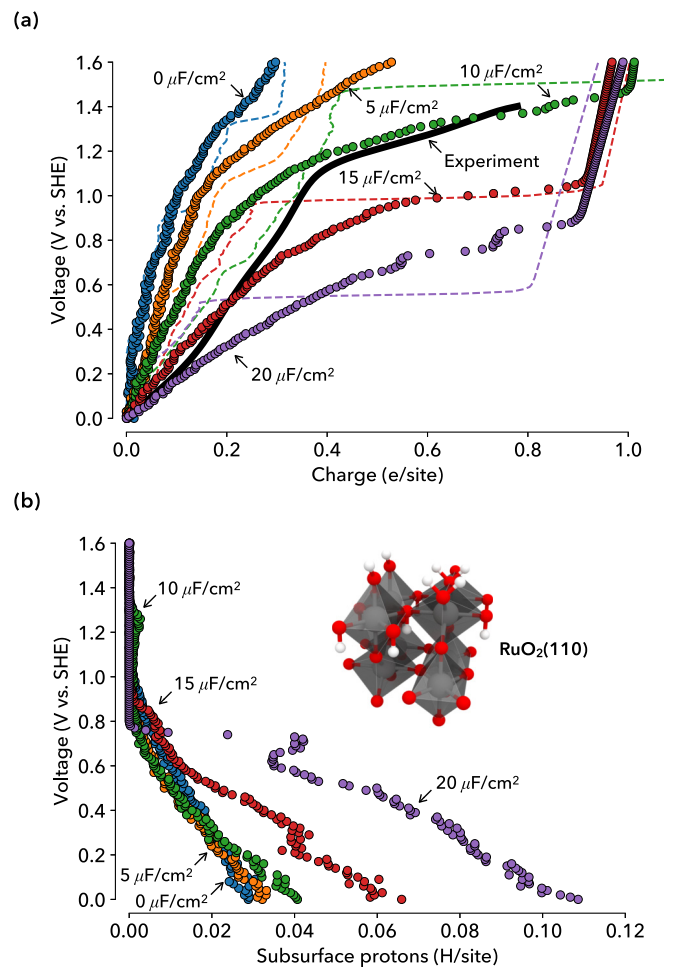


FIG. 3. Charge-voltage isotherms for the $RuO_2(110)$ surface obtained by electrochemical Monte Carlo sampling. (a) The dashed lines represent charge-voltage isotherms with no subsurface proton adsorption where the dots are calculations with subsurface adsorption. The change in slope between the two calculations demonstrates that including subsurface protons promotes a more typical pseudocapacitive response which is maximized at $20 \mu F/cm^2$. (b) Subsurface protons are allowed to exchange freely during simulations. As the double-layer capacitance increases, the amount of protons in the subsurface increase. When comparing with (a) it can be seen that this leads to a more linear response in the charge-voltage isotherm.

Subsurface adsorption leads to an increase in the pseudocapacitance due to the linear evolution of the charge-voltage response. This then implies that higher pseudocapacitive energy densities are achievable. It can then be inferred that promoting the stabilization of the subsurface protons lead to an increase in the energy capacity.

As the adsorption of sublayer protons increase the capacitance, it is of interest to understand how to maximize the energy-storage capabilities by promoting this process. To this end, we examine the response of the interface upon shifting the chemical potential of the subsurface proton to represent an additional stabilizing force in the sublayers. The shift in chemical potential is representative of local changes in the environment that would promote sublayer adsorption such as altering the solvent chemistry, applying a strain on the lattice,

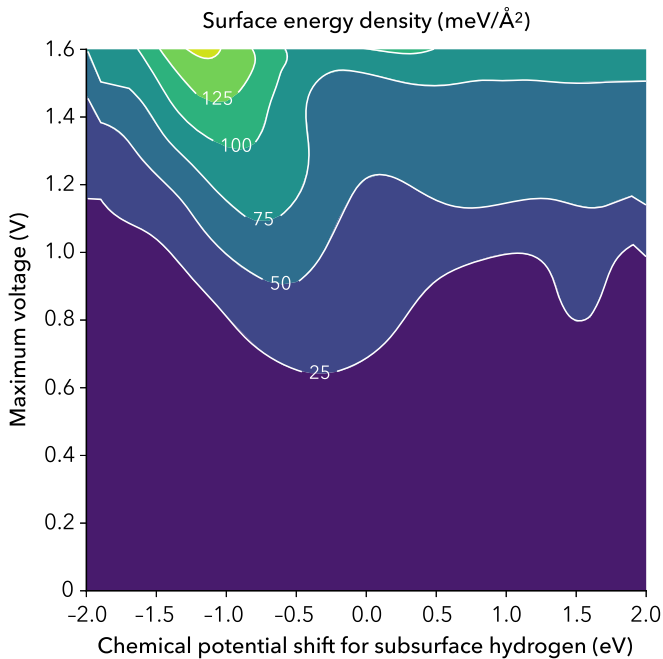


FIG. 4. Predicted energy densities in units of $\text{meV}/\text{\AA}^2$ for a protonated sublayer of the $\text{RuO}_2(110)$ surface. A varying chemical potential for the protons within the sublayer is included in the Hamiltonian. The maximized energy density was calculated using double-layer capacitances ranging from 0 to $20 \mu\text{F}/\text{cm}^2$.

or altering the chemistry of the sublayer with other dopants or metal atom substitution. A depiction of the maximum energy density as a function of the maximum applied voltage and the chemical potential of the subsurface protons is shown in Fig. 4. In this analysis we compute the energy density under a varying subsurface chemical potential. Initially at low voltages, the contributions of the subsurface chemical potential is minimal. With an increasing applied voltage, the necessary chemical potential shift becomes negative until it reaches $-1 \text{ eV}/\text{proton}$ producing a maximum energy density of $150 \text{ meV}/\text{\AA}^2$.

B. $\text{RuO}_2(101)$

To assess the transferability of the model to other surface facets, the $\text{RuO}_2(101)$ orientation was investigated. As seen in Fig. 1(b), the protons sit near the surface with some lower adsorption sites. During structure optimization, the RuO_2 structure undergoes slight reconstruction as protons reorient on the surface. For all calculations, no desorption process was observed leading to the conclusion that those configurations are stable. By enumerating the adsorption sites, 448 configurations were identified and computed. The electrochemical properties of those configurations are shown in Table A4 [34].

The free energy per adsorbed hydrogen is found to vary from -1.32 to -1.88 eV gradually until a coverage of 200% is reached. Configurational states that have coverages above 150% exhibit a PZC that lies below the stability window of an aqueous solution suggesting that higher coverages are not energetically favorable. A Helmholtz plane representing the ionic countercharge in contact with a charged surface is placed

at a distance of 3 \AA . The average double-layer capacitance is extracted yielding $\sim 10.9 \mu\text{F}/\text{cm}^2$ on a scale similar to the one previously calculated for $\text{RuO}_2(110)$ [6].

Using these data, the simulated adsorption isotherm for the (101) surface is shown in Fig. 5(b). Experimental CV measurements from Ref. [35] were converted to a charge-voltage curve that exhibits a linear response through the experimental voltage window. The neutral surface simulations exhibit a total discharge of $0.2e/\text{site}$ through the sampled voltage range where a small portion of the charge-voltage curve shows a linear response from 0.5 to 0.9 V vs SHE. In contrast, the charged surface simulations exhibit a linear response through the voltage window of 0–0.4 V vs SHE, indicative of a pseudocapacitive response. Additionally, the charged system exhibits minimal discharge from 0.4 to 1.4 V vs SHE followed by a batterylike discharge above this range.

In qualitative terms, the pseudocapacitive trend of the charged surface model is in agreement with the experimental linear response. This pseudocapacitive trend is not reproduced by the simulated neutral surface which instead exhibits minimal discharge from 0 to 0.5 V vs SHE at which point a slight hydrogen desorption is observed. From the charge-voltage response we can calculate the pseudocapacitance of the $\text{RuO}_2(101)$ facet which yields $200.3 \mu\text{F}/\text{cm}^2$ for the Monte Carlo simulations which is much lower than the value of $816.8 \mu\text{F}/\text{cm}^2$ obtained from experimental measurements. It is possible that the high scan rate (50 mV/s) of the CV measurements in Ref. [35] prevents the surface to reach thermodynamic equilibrium so that a direct comparison to the Monte Carlo data is not adequate. It has also been suggested in the literature that oxygen and hydroxyl desorption contribute to the pseudocapacitance and that including these mechanisms is needed to properly predict the adsorption isotherm [39]. Our model could be modified to accommodate these additional electrochemical processes albeit at a considerably higher computational cost.

C. $\text{RuO}_2(100)$

We now discuss the electrochemical response of the $\text{RuO}_2(100)$ surface. The properties of the 125 unique configurations used for the Monte Carlo simulations are recorded in Table A3 [34]. The preferred adsorption sites are the upper sites O_{up} . The next sites to be filled are the lower sites O_{low} which induce minimal lateral interactions between the protons on the surface. The PZC decreases gradually with the hydrogen coverage until reaching the reduction potential of water (0 V vs SHE) for a coverage of seven hydrogens per unit cell. This suggests that a coverage of eight protons per unit cell is not thermodynamically favorable under those conditions.

The free energy per adsorbed proton is found to vary from -1.3 to -2.25 eV with a linear decrease until a coverage of 150% where it becomes relatively constant. Additionally, the Fermi energy demonstrates a similar trend indicating that the surface has reached saturation. This is on a similar scale as previously reported for other RuO_2 surface facets [5,6].

We then perform Monte Carlo simulations to calculate the hydrogen-adsorption isotherm for a neutral and charged surfaces. Neutral surface calculations exhibit a moderate linear response through a voltage window of ~ 0 –0.2 V vs SHE

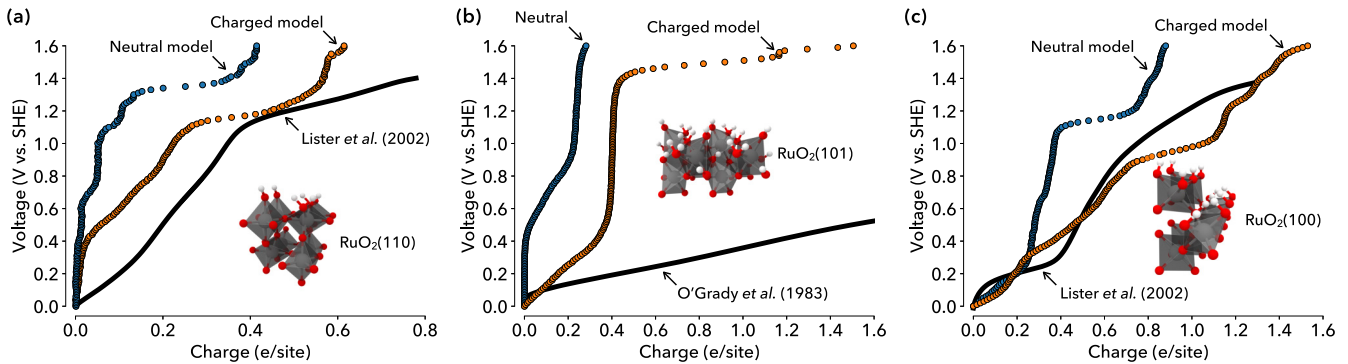


FIG. 5. The charge-voltage response for the (110), (101), and (100) surfaces of RuO_2 , respectively. The neutral (blue) and charged (orange) simulations are compared to experimental results taken from Ref. [11] for the (110) and (100) facets using a scan rate of 5 mV/s and Ref. [35] for the (101) facet using a scan rate of 50 mV/s.

followed by minimal discharge through 0.2–1.1 V vs SHE. A batterylike discharge is observed at 1.1 V vs SHE followed by a comparable discharge. In contrast, the simulations of the charged surface indicate a pseudocapacitive response across the stability window of water. We calculate the pseudocapacitance of the $\text{RuO}_2(100)$ facet which yields $207.7 \mu\text{F}/\text{cm}^2$ which is 12.7% larger than the experimentally observed value of $181.3 \mu\text{F}/\text{cm}^2$. Overall, we find the charged surface simulations to be in conclusive agreement with experiment.

IV. CONCLUSION

In this study we have presented a detailed analysis of the pseudocapacitive performance of the $\text{RuO}_2(110)$, (101), and (100) facets. We have found that simulations that do not incorporate the influence of the surface charge yield moderate pseudocapacitive discharge, maintaining a batterylike behavior through the stability window of water, whereas charged surface simulations capture the experimentally observed pseudocapacitive trends. We have studied the inclusion of subsurface protons along the (110) facet as a promising means to enhance the pseudocapacitive response of RuO_2 . The simulated adsorption isotherms for the (101) charged surface has been

shown to depart from experimental voltammetric data, yielding a capacitance of $200.3 \mu\text{F}/\text{cm}^2$ which underestimates the experimental value of $816.8 \mu\text{F}/\text{cm}^2$. This underestimation possibly originates from the fact that the high experimental scan rate prevents an accurate comparison between equilibrium Monte Carlo simulations and cyclic measurements or that oxygen and hydroxyl desorption affects the predicted pseudocapacitance. At variance with $\text{RuO}_2(101)$, the (100) surface shows qualitative and quantitative agreement with experimental data; the calculated pseudocapacitance equals $207.7 \mu\text{F}/\text{cm}^2$, which is in very good agreement with the experimental value of $181.3 \mu\text{F}/\text{cm}^2$. These results validate the accuracy of the proposed proton-adsorption model in the low-voltage region, while oxygen and hydroxyl adsorption is likely to control the pseudocapacitive response of $\text{RuO}_2(100)$ at high potential.

ACKNOWLEDGMENTS

The authors acknowledge financial support from Murata Manufacturing Co., Ltd. and the Center for Dielectrics and Piezoelectrics. We thank the Penn State Institute for CyberScience for providing high-performance computing resources and technical assistance throughout this work.

- [1] R. Kötz and M. Carlen, *Electrochim. Acta* **45**, 2483 (2000).
- [2] V. Augustyn, P. Simon, and B. Dunn, *Energy Environ. Sci.* **7**, 1597 (2014).
- [3] A. Muzaffar, M. B. Ahamed, K. Deshmukh, and J. Thirumalai, *Renew. Sust. Energ. Rev.* **101**, 123 (2019).
- [4] V. Ozolins, F. Zhou, and M. Asta, *Acc. Chem. Res.* **46**, 1084 (2013).
- [5] Y. Liu, F. Zhou, and V. Ozolins, *J. Phys. Chem. C* **116**, 1450 (2012).
- [6] N. Keilbart, Y. Okada, A. Feehan, S. Higai, and I. Dabo, *Phys. Rev. B* **95**, 115423 (2017).
- [7] C. Zhan, C. Lian, Y. Zhang, M. W. Thompson, Y. Xie, J. Wu, P. R. C. Kent, P. T. Cummings, D.-e. Jiang, and D. J. Wesolowski, *Adv. Sci.* **4**, 1700059 (2017).
- [8] C. Zhan and D.-e. Jiang, *J. Phys.: Condens. Matter* **28**, 464004 (2016).
- [9] C. Zhan, M. Naguib, M. Lukatskaya, P. R. C. Kent, Y. Gogotsi, and D.-e. Jiang, *J. Phys. Chem. Lett.* **9**, 1223 (2018).
- [10] C. Zhan, W. Sun, P. R. C. Kent, M. Naguib, Y. Gogotsi, and D.-e. Jiang, *J. Phys. Chem. C* **123**, 315 (2019).
- [11] T. E. Lister, Y. Chu, W. Cullen, H. You, R. M. Yonco, J. F. Mitchell, and Z. Nagy, *J. Electroanal. Chem.* **524-525**, 201 (2002).
- [12] E. Guerrini, V. Consonni, and S. Trasatti, *J. Solid State Electrochem.* **9**, 320 (2005).
- [13] Y. S. Chu, T. E. Lister, W. G. Cullen, H. You, and Z. Nagy, *Phys. Rev. Lett.* **86**, 3364 (2001).
- [14] W. Sugimoto, K. Yokoshima, Y. Murakami, and Y. Takasu, *Electrochim. Acta* **52**, 1742 (2006).

- [15] L. Y. Chen, Y. Hou, J. L. Kang, A. Hirata, T. Fujita, and M. W. Chen, *Adv. Energy Mater.* **3**, 851 (2013).
- [16] N. Yoshida, Y. Yamada, S.-i. Nishimura, Y. Oba, M. Ohnuma, and A. Yamada, *J. Phys. Chem. C* **117**, 12003 (2013).
- [17] O. Andreussi, I. Dabo, and N. Marzari, *J. Chem. Phys.* **136**, 064102 (2012).
- [18] S. E. Weitzner and I. Dabo, *npj Comput. Mater.* **3**, 1 (2017).
- [19] S. E. Weitzner and I. Dabo, *Phys. Rev. B* **96**, 205134 (2017).
- [20] Q. Campbell and I. Dabo, *Phys. Rev. B* **95**, 205308 (2017).
- [21] Q. Campbell, D. Fisher, and I. Dabo, *Phys. Rev. Mater.* **3**, 015404 (2019).
- [22] S. E. Weitzner and I. Dabo, *J. Chem. Phys.* **150**, 041715 (2019).
- [23] P. Giannozzi, S. Baroni, N. Bonini, M. Calandra, R. Car, C. Cavazzoni, D. Ceresoli, G. L. Chiarotti, M. Cococcioni, I. Dabo, A. Dal Corso, S. de Gironcoli, S. Fabris, G. Fratesi, R. Gebauer, U. Gerstmann, C. Gougoussis, A. Kokalj, M. Lazzeri, L. Martin-Samos, N. Marzari, F. Mauri, R. Mazzarello, S. Paolini, A. Pasquarello, L. Paulatto, C. Sbraccia, S. Scandolo, G. Sclauzero, A. P. Seitsonen, A. Smogunov, P. Umari, and R. M. Wentzcovitch, *J. Phys.: Condens. Matter* **21**, 395502 (2009).
- [24] J. P. Perdew, K. Burke, and M. Ernzerhof, *Phys. Rev. Lett.* **77**, 3865 (1996).
- [25] N. Marzari, D. Vanderbilt, A. De Vita, and M. C. Payne, *Phys. Rev. Lett.* **82**, 3296 (1999).
- [26] P. Giannozzi, O. Andreussi, T. Brumme, O. Bunau, M. B. Nardelli, M. Calandra, R. Car, C. Cavazzoni, D. Ceresoli, M. Cococcioni, N. Colonna, I. Carnimeo, A. D. Corso, S. de Gironcoli, P. Delugas, R. A. DiStasio, A. Ferretti, A. Floris, G. Fratesi, G. Fugallo, R. Gebauer, U. Gerstmann, F. Giustino, T. Gorni, J. Jia, M. Kawamura, H.-Y. Ko, A. Kokalj, E. Küçükbenli, M. Lazzeri, M. Marsili, N. Marzari, F. Mauri, N. L. Nguyen, H.-V. Nguyen, A. O. de-la Roza, L. Paulatto, S. Poncé, D. Rocca, R. Sabatini, B. Santra, M. Schlipf, A. P. Seitsonen, A. Smogunov, I. Timrov, T. Thonhauser, P. Umari, N. Vast, X. Wu, and S. Baroni, *J. Phys.: Condens. Matter* **29**, 465901 (2017).
- [27] M. Knapp, D. Crihan, A. P. Seitsonen, E. Lundgren, A. Resta, J. N. Andersen, M. Curie, and P. Jussieu, *J. Phys. Chem. C* **111**, 5363 (2007).
- [28] H. Wang, W. F. Schneider, and D. Schmidt, *J. Phys. Chem. C* **113**, 15266 (2009).
- [29] K. Reuter and M. Scheffler, *Phys. Rev. B* **65**, 035406 (2001).
- [30] J. K. Nørskov, J. Rossmeisl, A. Logadottir, L. Lindqvist, J. R. Kitchin, T. Bligaard, and H. Jónsson, *J. Phys. Chem. B* **108**, 17886 (2004).
- [31] V. Stamenkovic, B. S. Mun, K. J. Mayrhofer, P. N. Ross, N. M. Markovic, J. Rossmeisl, J. Greeley, and J. K. Nørskov, *Angew. Chem. Int. Ed.* **45**, 2897 (2006).
- [32] H. Oberhofer, *Handbook of Materials Modeling: Applications: Current and Emerging Materials* (Springer International Publishing, 2018), p. 1.
- [33] K. S. Exner, *ChemSusChem* **12**, 2330 (2019).
- [34] See Supplemental Material at <http://link.aps.org/supplemental/10.1103/PhysRevMaterials.3.085405> for dataset of material properties used in Monte Carlo sampling.
- [35] W. E. O'Grady, A. K. Goel, F. H. Pollak, H. L. Park, and Y. S. Huang, *J. Electroanal. Chem.* **151**, 295 (1983).
- [36] L. M. Doubova, S. Daolio, A. D. Battisti, and L. M. Doubo, *J. Electroanal. Chem.* **532**, 25 (2002).
- [37] P. R. Bandaru, H. Yamada, R. Narayanan, and M. Hoefler, *Mater. Sci. Eng. R Rep.* **96**, 1 (2015).
- [38] S. Ardizzone, G. Fregonara, and S. Trasatti, *Electrochim. Acta* **35**, 263 (1990).
- [39] H. Over, *Chem. Rev.* **112**, 3356 (2012).
- [40] J. Rishpon and S. Gottesfeld, *J. Electrochem. Soc.* **131**, 1960 (1984).